

# Coupled-waveguides for dispersion compensation in semiconductor lasers

Yves Bidaux,<sup>a</sup> Filippos Kapsalidis, Pierre Jouy, Mattias Beck, and Jérôme Faist<sup>b</sup>

<sup>1</sup>*Institute for Quantum Electronics, ETH-Zurich, CH-8093 Zurich, Switzerland*

(Dated: January 7, 2022)

The generation of optical frequency combs via direct electrical pumping of semiconductor lasers [1–5] is an attractive alternative to the well-established mode-locked laser sources in terms of compactness, robustness and integrability. However, the high chromatic dispersion of bulk semiconductor materials [6] can prevent the generation of frequency combs [7] or lead to undesired pulse lengthening [8]. In this letter, we present a novel dual waveguide for intracavity dispersion compensation in semiconductor lasers. We apply the concept to a short mid-infrared wavelength quantum cascade laser operating in the first atmospheric window ( $\lambda \approx 4.6 \mu\text{m}$ ). As a result, stable comb operation on the full dynamical range is achieved in this device. Unlike previously proposed schemes, the dual waveguide approach can be applied to various types of semiconductor lasers and material systems. In particular, it could enable efficient group velocity dispersion compensation at near-infrared wavelengths where semiconductor materials exhibit a large value of that parameter.

Recently, novel sensing methods based on optical frequency combs [9] have attracted much attention. In particular, the dual comb configuration offers, for spectroscopy, the key advantage of combining high resolution with large spectral coverage while not requiring any moving part [10]. Quantum cascade lasers (QCLs) can operate as optical frequency combs [5, 11, 12] enabling the realization of compact mid-infrared dual-comb spectrometers [13–15]. The signal over noise characteristics of dual comb spectrometers heavily depend on the linewidth and stability of the comb devices. Recent experiments where Gires-Tournois dielectric coatings were deposited on the back facet of QCL devices showed the essential role of dispersion compensation for the improvement of the combs bandwidth and operation stability [7, 16]. However, dispersion compensation by waveguide engineering [17, 18] is preferable in terms of its capability to correct for large amounts of dispersion, as well as its reliability and cost.

In a coupled-waveguide system, the wavelength dependence of the inter-waveguide coupling through the evanescent tails of the individual modes may lead to a significant change of its propagation vector. In turn, the modes of coupled-waveguides can exhibit an additional dispersion that exceeds the one of bulk materials [19]. In

a previous work, we found that the coupling of the laser fundamental mode to a plasmonic resonance engineered in the lasers top cladding can lead to efficient dispersion compensation in long ( $\lambda \approx 7 \mu\text{m}$ ) mid-infrared wavelength QCLs [20, 21]. This approach cannot be applied to shorter wavelengths where dispersion is particularly high due to the proximity of the bandgap [22]. This is due to the difficulty to scale the plasma frequency accordingly (see Supplementary Fig. 1) and to the introduction of unavoidable free carrier losses.

In the present work, we demonstrate dispersion compensation by coupling the optical mode to a passive dielectric waveguide engineered in the device top cladding. We fabricated a QCL based on a diagonal three quantum well design for emission at  $4.6 \mu\text{m}$  [23, 24]. As seen in Fig. 1a, the device integrates a passive InGaAs waveguide close to the active region (see Methods for fabrication details). A Scanning Electron Micrograph (SEM) image of the device front facet is displayed in Fig. 1b. Naturally, each waveguide has a frequency-dependent propagation vector. The waveguides are designed such that these two propagation vectors are equal for a resonant frequency  $\omega_0$ . At this frequency, if the two optical modes have equal group velocity dispersion (GVD), these couple to form a symmetric and an anti-symmetric supermode with resonantly depressed (respectively enhanced) GVD that can then be used for dispersion compensation [19]. Applying directly such approach to a laser system leads to a fundamental difficulty: Since at resonance the supermodes are equally distributed in both waveguides, lasing can occur on the high and low GVD supermodes simultaneously.

We therefore considered a system where the two modes of the individual waveguides have a different GVD. In that case, using coupled mode theory, the induced GVD ( $\Delta\text{GVD}$ ) writes as (see Supplementary materials for the derivation):

$$\Delta\text{GVD}_{+/-} \simeq \pm \frac{\kappa}{\delta\omega^2} (\tilde{\omega}^2 + 1)^{-3/2} (1 + \alpha\tilde{\omega}) \quad (1)$$

for the symmetric (+) and anti-symmetric (-) modes, where  $\kappa$  is the coupling strength,  $\tilde{\omega} = (\omega - \omega_0)/\delta\omega$  is the normalised frequency,  $\delta\omega = 2\kappa \left| \frac{1}{\nu_1} - \frac{1}{\nu_2} \right|^{-1}$  the resonance bandwidth and  $\alpha = \frac{6\kappa}{\delta\omega^2} (D_1 - D_2)$  the asymmetry factor. In the last expressions,  $\nu_i$  are the group velocities and  $D_i$  the GVDs of the decoupled active region ( $i=1$ ) and passive waveguide ( $i=2$ ) modes. For  $\alpha$  different from zero, the GVD difference between the two waveguides  $D_1 - D_2$  induces a shift of the GVD maxima. In turn, dispersion compensation can be achieved without requiring that the two optical modes are in resonance. The resulting asymmetry in the overlap factor of the two

<sup>a</sup> bidauxy@phys.ethz.ch

<sup>b</sup> jfaist@ethz.ch

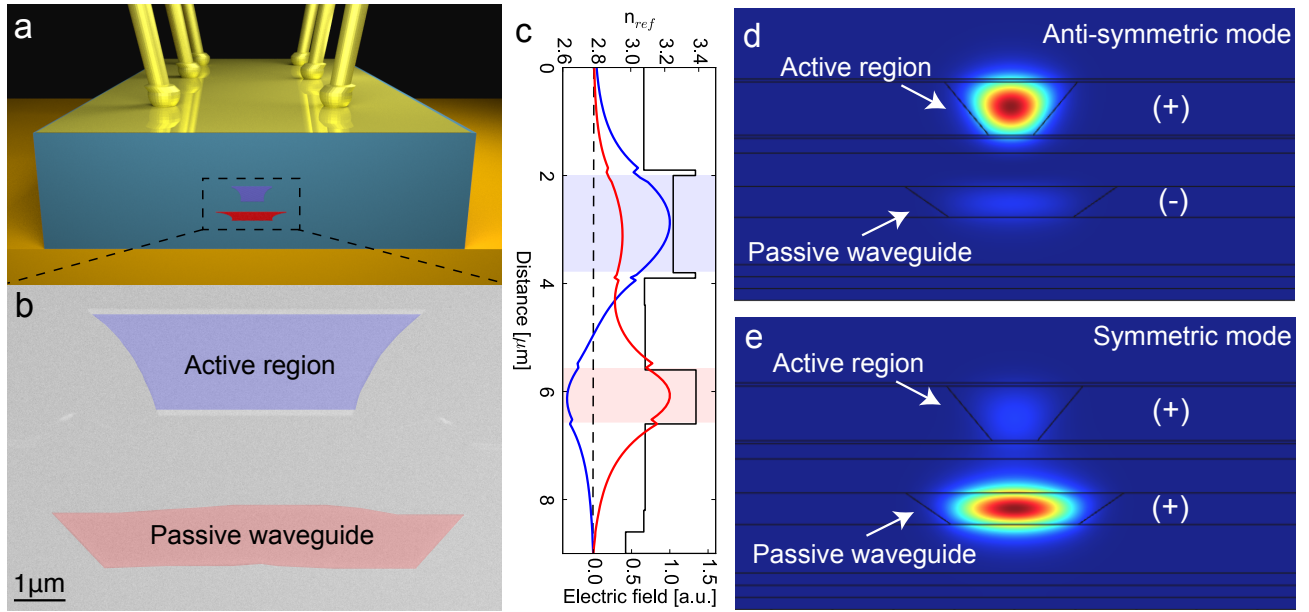


FIG. 1. **Device cross-section.** **a**, Schematic view of a mounted device. **b**, SEM picture of the fabricated device. The passive waveguide is coloured with red while the active region is coloured in blue. **c**, Cut in the vertical plane of the electric field profile of the anti-symmetric (blue line) and symmetric (red line) modes and refractive index profiles. **d**, Intensity profile of the anti-symmetric mode at  $2220 \text{ cm}^{-1}$ . **e**, Intensity profile of the symmetric mode at  $2220 \text{ cm}^{-1}$ .

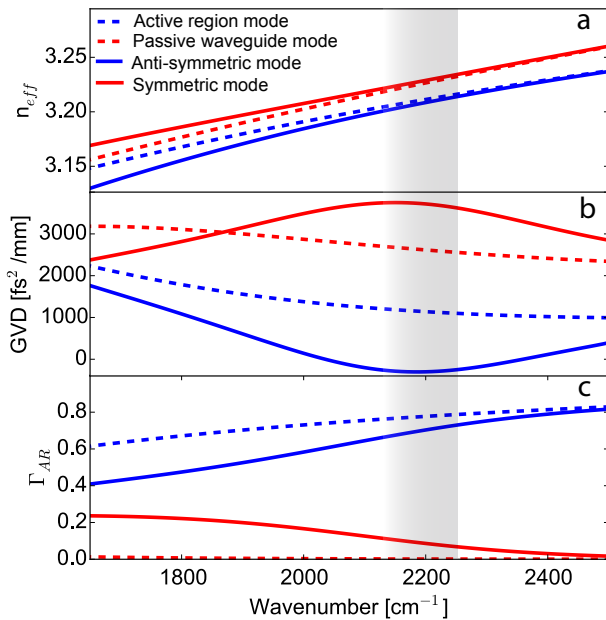


FIG. 2. **Simulation of the dispersion.** **a**, Effective refractive index, **b**, GVD as a function of frequency and **c**, overlap factor for the active region (dashed blue line), passive waveguide (dashed red line), anti-symmetric (blue line) and symmetric (red line) modes.

supermodes with the active region enables the laser to naturally select one of the two and remain monomode.

We simulated the optical modes for various geometries using a finite element solver (see Methods) and targeted zero GVD at the central laser wavelength. The refractive

index profile along the growth axis of the fabricated device is displayed in Fig. 1c. The computed electric field profile of the anti-symmetric (blue line) and symmetric (red line) modes are also displayed, while the full two dimensional intensity profiles of these modes are reported in Fig. 1d and e. These two modes result from the coupling of the two distinct active region and passive waveguide optical modes with GVD  $D_1 = 1140 \text{ fs}^2/\text{mm}$  and  $D_2 = 2600 \text{ fs}^2/\text{mm}$ . The dispersion curves of the two uncoupled modes are reported in Fig. 2a with dashed lines while the dispersion of the coupled modes are reported with full lines. Our simulation predicts a minimum of the GVD close to zero at the laser operation wavelength for the anti-symmetric mode (see Fig. 2b, shaded area) and an overlap with the active region equal to 0.7 (see Fig. 2c). The latter has as a result a much larger overlap with the active region ( $\Gamma_{AR}$ ) than the symmetric mode which is localized in the passive waveguide. This induces a strong mode selection mechanism which ensures that the device operates with high efficiency on the low GVD anti-symmetric mode.

To confirm that the laser operates on the anti-symmetric mode, we measured its farfield emission profile in pulsed operation at rollover. These experimental data (see Fig. 3a) are compared to the farfield computed from the supermodes nearfield obtained from our 2D mode simulation that are displayed in Fig. 3b-c. The difference between the measured (Fig. 3a) and computed (Fig. 3c) farfield is attributed to the presence of loss and gain in the passive waveguide and active region, respectively, which is not taken into account by our model.

We measured the light and voltage versus current characteristics of the device while operated under continuous

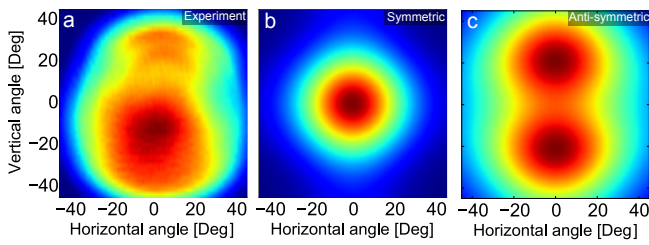


FIG. 3. **Farfield.** **a**, Farfield emission profile of the device measured in pulsed mode for a current of 830 mA. **b-c**, Simulated farfield emission profile for the symmetric and the anti-symmetric modes.

wave operation at  $-15\text{ }^{\circ}\text{C}$ . The output power reached 75 mW at rollover (see Fig. 4a). We deduced the GVD from the subthreshold emission spectrum [25] measured at a current of 450 mA at  $-15\text{ }^{\circ}\text{C}$ . The GVD is displayed in Fig. 4b (red line). For comparison, a measurement performed on a 4.5 mm long reference device without the additional passive waveguide (see Methods for fabrication details and Supplementary Fig. 2 for full characterization) is also displayed (blue line). For the reference device, a GVD as large as  $740\text{ fs}^2/\text{mm}$  is deduced at  $2200\text{ cm}^{-1}$ , while for the device including the passive waveguide a GVD of only  $50\text{ fs}^2/\text{mm}$  is deduced at  $2200\text{ cm}^{-1}$ . This confirms that the coupling to the passive waveguide reduced the dispersion of the device ( $\Delta\text{GVD} = -690\text{ fs}^2/\text{mm}$ ).

To characterize the coherence of the optical spectrum we measured the intermode beatnote of the device directly from the laser bias current using a RF spectrum analyzer [13] with a resolution bandwidth (RBW) of 500 Hz. Narrow beatnotes with full width at half maximum (FWHM) less than 500 Hz were measured on the whole dynamical range (see Fig. 4c and Supplementary Fig. 3). The intermode beatnote frequency tuned smoothly with current at a rate of  $-0.13\text{ GHz/A}$ , similar to values reported in Bidaux *et al.* [20]. At a current of 830 mA the intermode beatnote has a FWHM  $\simeq 411\text{ Hz}$  (Fig. 4d) and the optical spectrum spans  $40\text{ cm}^{-1}$  (see Fig. 4e). Such narrow and stable beatnotes have up to now always been observed in QCLs operating in comb regime.

Nevertheless, to demonstrate that the devices actually operate as frequency combs, we measured the multiheterodyne beating spectrum of two HR coated 4 mm devices at  $-20\text{ }^{\circ}\text{C}$ . The first device current was set to 600 mA while the second device current was set to 460 mA. The optical beams were combined and focused on a MCT detector and the signal was recorded using an oscilloscope. The total acquisition time was 40 ms and the signal was averaged with a single acquisition time of  $3.3\text{ }\mu\text{s}$  using the method detailed in Villares *et al.* [13]. The resulting spectrum is displayed in Fig. 4f. Ninety three distinct comb lines are observed. Since the free spectral range of the combs is approximately  $0.39\text{ cm}^{-1}$ , this corresponds to an optical span of  $38\text{ cm}^{-1}$  and demonstrates that the devices operate as frequency combs on

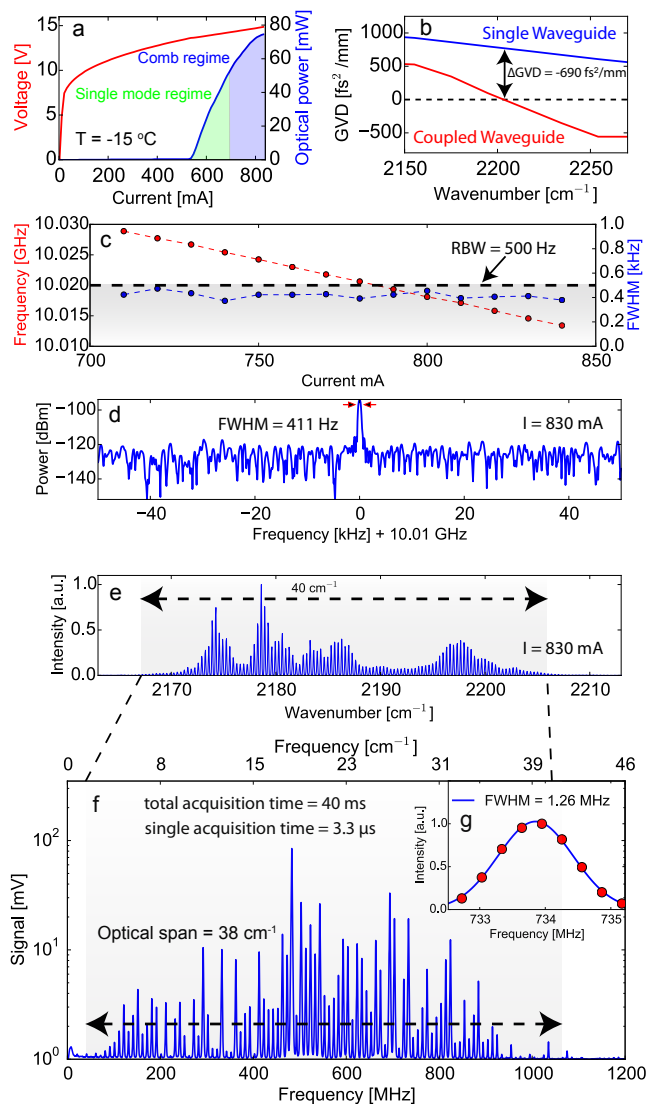


FIG. 4. **Frequency combs characterization.** **a**, Light and voltage versus current characteristics of the device measured at  $-15\text{ }^{\circ}\text{C}$  in continuous wave. **b**, GVD measured at  $-15\text{ }^{\circ}\text{C}$  for a current of 450 mA for the device (red line) and for a current of 265 mA for the reference device (blue line). **c**, Intermode beatnote frequency (blue) and FWHM (red) as a function of current measured at  $-15\text{ }^{\circ}\text{C}$  with a resolution bandwidth of 500 Hz. **d**, Intermode beatnote measured at  $-15\text{ }^{\circ}\text{C}$  for a current of 830 mA. **e**, Optical spectrum measured in continuous wave at  $-15\text{ }^{\circ}\text{C}$  for a current of 830 mA. **f**, Multiheterodyne beating spectrum of the two frequency combs. 93 distinct comb lines can be seen corresponding to an optical span of  $38\text{ cm}^{-1}$ . **g**, The FWHM of one line is 1.26 MHz.

the whole spectral bandwidth. The FWHM of one line is 1.26 MHz (see Fig. 4g), this directly shows the suitability of these devices for dual-comb spectrometers in the first atmospheric window.

In conclusion, we presented a dual coupled-waveguide design for dispersion compensation in semiconductor lasers and demonstrated its application to a quantum cas-

cade laser. The fabricated devices operate as frequency combs on the whole spectral bandwidth and dynamical range. Unlike previously demonstrated integrated dispersion compensation methods, the dual waveguide scheme can be applied to various types of semiconductor lasers and material systems. Moreover, it allows to correct for GVD values up to a few thousand  $\text{fs}^2/\text{mm}$ . This suggests that this design strategy could enable the development of high performance semiconductor laser based optical frequency combs from the long mid-infrared to the near-infrared wavelengths ranges. Actually, an interband laser waveguide design that is computed to be dispersion compensated at  $1.3 \mu\text{m}$  is proposed in the supplementary material.

## METHODS

### Devices fabrication

The active region of the device including coupled-waveguides was grown by molecular beam epitaxy using the InGaAs/AlInAs material system on an InP:Si ( $2 \times 10^{17} \text{ cm}^{-3}$ ) substrate. The active layers were placed between two 100 nm thin layers of Si-doped InGaAs ( $6 \times 10^{16} \text{ cm}^{-3}$ ). The exact layers sequence of the QCL is detailed in Yang *et al.* [23]. The device was processed to a buried heterostructure QCL. A  $4.4 \mu\text{m}$  wide ridge was

etched by wet-etching technique and a lateral InP:Fe insulating layer was grown by metalorganic vapour phase epitaxy (MOVPE). The top cladding layers were then grown by MOVPE and include an InGaAs waveguiding layer. The top cladding layers sequence is  $0.5 \mu\text{m}$  InP:Si  $1 \times 10^{17} \text{ cm}^{-3}$ ,  $1.2 \mu\text{m}$  InP:Si  $1 \times 10^{16} \text{ cm}^{-3}$ ,  $1 \mu\text{m}$  InGaAs:Si  $1 \times 10^{16} \text{ cm}^{-3}$ ,  $1.6 \mu\text{m}$  InP:Si  $1 \times 10^{16} \text{ cm}^{-3}$ ,  $0.4 \mu\text{m}$  InP:Si  $2 \times 10^{17} \text{ cm}^{-3}$ ,  $0.4 \mu\text{m}$  InP:Si  $3 \times 10^{18} \text{ cm}^{-3}$ . A second  $6.7 \mu\text{m}$  wide ridge was etched in the cladding by wet-etching and a lateral InP:Fe insulating layer was grown by MOVPE. For the reference device the top cladding layers sequence is:  $0.42 \mu\text{m}$  InP:Si  $1 \times 10^{17} \text{ cm}^{-3}$ ,  $2.5 \mu\text{m}$  InP:Si  $1 \times 10^{16} \text{ cm}^{-3}$ ,  $0.85 \mu\text{m}$  InP:Si  $1 \times 10^{18} \text{ cm}^{-3}$ . Devices were mounted episcide down on AlN submounts.

### Optical mode simulation

We performed two-dimensional finite-element simulations of the waveguide structure using the commercially available software Comsol Multiphysics. The intrinsic refractive indices were obtained from Pikhtin and Yas'kov formula using the parameters given in Palik and Ghosh [6]. The doped refractive indices are deduced using Drude model. We assume a collision time of 100 fs and effective masses of  $0.073 m_e$  for InP and  $0.043 m_e$  for InGaAs.

- 
- [1] D. J. Derickson, R. J. Helkey, A. Mar, J. R. Karin, J. G. Wasserbauer, and J. E. Bowers, "Short pulse generation using multisegment mode-locked semiconductor lasers," *IEEE Journal of Quantum Electronics* **28**, 2186–2202 (1992).
  - [2] E. Avrutin, J. Marsh, and E. Portnoi, "Monolithic and multi-GigaHertz mode-locked semiconductor lasers: Constructions, experiments, models and applications," *IEE Proceedings - Optoelectronics* **147**, 251–278 (2000).
  - [3] U. Keller and A. C. Tropper, "Passively modelocked surface-emitting semiconductor lasers," *Physics Reports* **429**, 67–120 (2006).
  - [4] E. U. Rafailov, M. A. Cataluna, and W. Sibbett, "Mode-locked quantum-dot lasers," *Nature photonics* **1**, 395–401 (2007).
  - [5] A. Hugi, G. Villares, S. Blaser, H. C. Liu, and J. Faist, "Mid-infrared frequency comb based on a quantum cascade laser," *Nature* **492**, 229–233 (2012).
  - [6] E. D. Palik and G. Ghosh, eds., *Handbook of optical constants of solids* (Academic Press, San Diego, 1998).
  - [7] G. Villares, S. Riedi, J. Wolf, D. Kazakov, M. J. Süess, P. Jouy, M. Beck, and J. Faist, "Dispersion engineering of quantum cascade laser frequency combs," *Optica* **3**, 252 (2016).
  - [8] J. Kim, M.-T. Choi, and P. J. Delfyett, "Pulse generation and compression via ground and excited states from a grating coupled passively mode-locked quantum dot two-section diode laser," *Applied Physics Letters* **89**, 261106 (2006).
  - [9] S. A. Diddams, "The evolving optical frequency comb [Invited]," *Journal of the Optical Society of America B* **27**, B51 (2010).
  - [10] F. Keilmann, C. Gohle, and R. Holzwarth, "Time-domain mid-infrared frequency-comb spectrometer," *Optics letters* **29**, 1542–1544 (2004).
  - [11] M. Rösch, G. Scalari, M. Beck, and J. Faist, "Octave-spanning semiconductor laser," *Nature Photonics*, 42–47 (2014).
  - [12] D. Burghoff, T.-Y. Kao, N. Han, C. W. I. Chan, X. Cai, Y. Yang, D. J. Hayton, J.-R. Gao, J. L. Reno, and Q. Hu, "Terahertz laser frequency combs," *Nature Photonics* **8**, 462–467 (2014).
  - [13] G. Villares, A. Hugi, S. Blaser, and J. Faist, "Dual-comb spectroscopy based on quantum-cascade-laser frequency combs," *Nature Communications* **5**, 5192 (2014).
  - [14] Y. Yang, D. Burghoff, D. J. Hayton, J.-R. Gao, J. L. Reno, and Q. Hu, "Terahertz multiheterodyne spectroscopy using laser frequency combs," *Optica* **3**, 499 (2016).
  - [15] J. Westberg, L. A. Sterczewski, and G. Wysocki, "Mid-infrared multiheterodyne spectroscopy with phase-locked quantum cascade lasers," *Applied Physics Letters* **110**, 141108 (2017).
  - [16] Q. Y. Lu, S. Manna, S. Slivken, D. H. Wu, and M. Razeghi, "Dispersion compensated mid-infrared quantum cascade laser frequency comb with high power output," *AIP Advances* **7**, 045313 (2017).
  - [17] J. Riemensberger, K. Hartinger, T. Herr, V. Brasch, R. Holzwarth, and T. J. Kippenberg, "Dispersion en-

- gineering of thick high-Q silicon nitride ring-resonators via atomic layer deposition,” *Optics Express* **20**, 27661 (2012).
- [18] Y. Okawachi, M. R. E. Lamont, K. Luke, D. O. Carvalho, M. Yu, M. Lipson, and A. L. Gaeta, “Bandwidth shaping of microresonator-based frequency combs via dispersion engineering,” *Optics Letters* **39**, 3535 (2014).
- [19] U. Peschel, T. Peschel, and F. Lederer, “A compact device for highly efficient dispersion compensation in fiber transmission,” *Applied Physics Letters* **67**, 2111 (1995).
- [20] Y. Bidaux, I. Sergachev, W. Wuester, R. Maulini, T. Gresch, A. Bismuto, S. Blaser, A. Muller, and J. Faist, “Plasmon-enhanced waveguide for dispersion compensation in mid-infrared quantum cascade laser frequency combs,” *Optics Letters* **42**, 1604 (2017).
- [21] P. Jouy, J. M. Wolf, Y. Bidaux, P. Allmendinger, M. Mangold, M. Beck, and J. Faist, “Dual comb operation of  $\lambda$  8.2  $\mu\text{m}$  Quantum Cascade Laser frequency comb with 1 W optical power,” *Applied Physics Letters* **111**, 141102 (2017).
- [22] Y. Bidaux, K. A. Fedorova, D. A. Livshits, E. U. Rafailov, and J. Faist, “Investigation of the chromatic dispersion in two-section InAs/GaAs quantum-dot lasers,” *IEEE Photonics Technology Letters* **29**, 2246 – 2249 (2017).
- [23] Q. Yang, R. Lösch, W. Bronner, S. Hugger, F. Fuchs, R. Aidam, and J. Wagner, “High-peak-power strain-compensated GaInAs/AlInAs quantum cascade lasers (4.6  $\mu\text{m}$ ) based on a slightly diagonal active region design,” *Applied Physics Letters* **93**, 251110 (2008).
- [24] A. Bismuto, R. Terazzi, M. Beck, and J. Faist, “Influence of the growth temperature on the performances of strain-balanced quantum cascade lasers,” *Applied Physics Letters* **98**, 091105 (2011).
- [25] D. Hofstetter and J. Faist, “Measurement of semiconductor laser gain and dispersion curves utilizing Fourier transforms of the emission spectra,” *IEEE Photonics Technology Letters* **11**, 1372–1374 (1999).

## ACKNOWLEDGEMENTS

The authors would like to thank Dmitry Kazakov and Matthew Singleton for careful reading of the paper and fruitful discussions. This work was supported by the Swiss National Science Foundation (SNF) and by DARPA under the SCOUT program.

## AUTHORS CONTRIBUTIONS

Y.B. developed the simulations, designed the waveguide, performed experiments, analysed data and wrote the manuscript. F.K. fabricated the coupled-waveguide quantum cascade lasers, performed experiments and analysed data. P.J. fabricated the reference quantum cascade lasers, performed experiments and analysed data. M.B. grew the quantum cascade laser material. J.F. proposed the experiment, analysed data and supervised the work.

# Coupled waveguides for dispersion compensation in semiconductor lasers: Supplementary materials

Yves Bidaux,<sup>a</sup> Filippos Kapsalidis, Pierre Jouy, Mattias Beck, and Jérôme Faist<sup>b</sup>

<sup>1</sup>*Institute for Quantum Electronics, ETH-Zurich, CH-8093 Zurich, Switzerland*

(Dated: January 7, 2022)

arXiv:1711.09116v1 [physics.optics] 24 Nov 2017

---

<sup>a</sup> bidauxy@phys.ethz.ch

<sup>b</sup> jfaist@ethz.ch

## PLASMA FREQUENCY

The plasma frequency [1] is shown as a function of the carrier density for InP and InGaAs in Supplementary Fig. 1. To fabricate a dispersion compensated QCL frequency comb based on a plasmon enhanced waveguide at  $4.6 \mu\text{m}$  the doping concentration of the plasmonic layer should be increased to more than  $10^{20} \text{ cm}^{-3}$  which cannot be realised in practice. Therefore, for short infrared wavelengths this approach cannot be used.

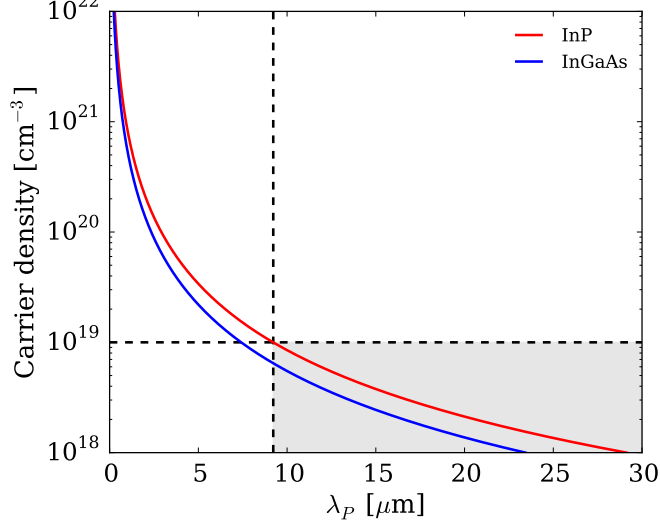


FIG. 1. **Plasma frequency:** Plasma frequency as a function of the carrier density for InP and InGaAs.

## COUPLED MODE THEORY

A model describing the dispersion of coupled waveguides and based on the coupled mode theory was proposed by Peschel et al. [2] The decoupled active region ( $i=1$ ) and passive waveguide ( $i=2$ ) modes have propagation constants  $\beta_{1,2}$ , group velocity  $\nu_{1,2}$  and GVD  $D_{1,2}$ . The propagation vectors can be expanded around the frequency  $\omega_0$  at which the propagation vectors are phase matched as

$$\beta_i(\omega) = \beta_0(\omega) + (\omega - \omega_0) \frac{1}{\nu_i} + \frac{1}{2} (\omega - \omega_0)^2 D_i. \quad (1)$$

The modes of the coupled system are given by the eigensolutions of the matrix  $M$ :

$$\frac{da}{dz} = -Ma = - \begin{pmatrix} \delta & \kappa \\ \kappa & -\delta \end{pmatrix} \cdot \begin{pmatrix} a_1 \\ a_2 \end{pmatrix}, \quad (2)$$

with  $\delta = (\beta_1 - \beta_2)/2$ ,  $a_i$  the amplitudes of the modes and  $\kappa$  the coupling constant between the two modes. The two optical modes couple to form two symmetric (+) and anti-symmetric (-) supermodes with propagation constants given by:

$$\beta_{\pm} = \frac{1}{2} (\beta_1 + \beta_2) \pm \sqrt{\kappa^2 + (\beta_1 - \beta_2)^2 / 4}. \quad (3)$$

If the modes have the same GVD ( $GVD_0$ ), defining  $\tilde{\omega} = \frac{(\omega - \omega_0)}{\delta\omega}$  where  $\delta\omega = 2\kappa \left| \frac{1}{\nu_1} - \frac{1}{\nu_2} \right|^{-1}$  one gets

$$\beta'_{+/-} = \frac{1}{2} \left( \frac{1}{\nu_1} + \frac{1}{\nu_2} \right) + (\omega - \omega_0) GVD_0 \pm \frac{\kappa \tilde{\omega}}{\delta\omega} (\tilde{\omega}^2 + 1)^{1/2} \quad (4)$$

and

$$\beta''_{+/-} = GVD_0 \pm \frac{\kappa}{\delta\omega^2} \left[ (\tilde{\omega}^2 + 1)^{-1/2} - \tilde{\omega}^2 (\tilde{\omega}^2 + 1)^{-3/2} \right] = GVD_0 \pm \frac{\kappa}{\delta\omega^2} (\tilde{\omega}^2 + 1)^{-3/2} \quad (5)$$

and the GVD of the supermodes is

$$\text{GVD}_{+/-} = \text{GVD}_0 \pm \frac{1}{4\kappa} \left( \frac{1}{\nu_1} - \frac{1}{\nu_2} \right) (\tilde{\omega}^2 + 1)^{-3/2}. \quad (6)$$

The GVD induced by the coupling ( $\kappa$ ) is positive for the symmetric mode and negative for the anti-symmetric mode. At  $\omega_0$  the induced GVD is maximal and equals

$$\text{GVD}_{+/-}^{peak} = \text{GVD}_0 \pm \frac{1}{4\kappa} \left( \frac{1}{\nu_1} - \frac{1}{\nu_2} \right)^2. \quad (7)$$

If the two modes now have a dissimilar GVD, the solution is given by

$$\begin{aligned} \text{GVD}_{+/-} = & \frac{1}{2} (D_1 + D_2) \\ & \pm \frac{-\kappa^2 \tilde{\omega}^2 \left[ (\nu_1 - \nu_2)^2 + 2(D_1 - D_2) \nu_1^2 \nu_2^2 \kappa \tilde{\omega} \right]^2 \left[ (\nu_1 - \nu_2)^2 + (D_1 - D_2) \nu_1^2 \nu_2^2 \kappa \tilde{\omega} \right]}{\nu_1^2 \nu_2^2 (\nu_1 - \nu_2)^6 \left( 1 + \frac{\tilde{\omega}^2}{(\nu_1 - \nu_2)^4} \left[ (\nu_1 - \nu_2)^2 + (D_1 - D_2) \nu_1^2 \nu_2^2 \kappa \tilde{\omega} \right]^2 \right)^{3/2}} \\ & \pm \frac{\left[ (\nu_1 - \nu_2)^2 + (D_1 - D_2) \nu_1^2 \nu_2^2 \kappa \tilde{\omega} \right]^2}{\nu_1^2 \nu_2^2 (\nu_1 - \nu_2)^2 \kappa \sqrt{1 + \frac{\tilde{\omega}^2}{(\nu_1 - \nu_2)^4} \left[ (\nu_1 - \nu_2)^2 + (D_1 - D_2) \nu_1^2 \nu_2^2 \kappa \tilde{\omega} \right]^2}} \\ & \pm \frac{2(D_1 - D_2) \tilde{\omega} \left[ (\nu_1 - \nu_2)^2 + (D_1 - D_2) \nu_1^2 \nu_2^2 \kappa \tilde{\omega} \right]}{(\nu_1 - \nu_2)^2 \kappa \sqrt{1 + \frac{\tilde{\omega}^2}{(\nu_1 - \nu_2)^4} \left[ (\nu_1 - \nu_2)^2 + (D_1 - D_2) \nu_1^2 \nu_2^2 \kappa \tilde{\omega} \right]^2}}. \quad (8) \end{aligned}$$

One can express the full solution under the form of equation 6 by reorganizing the terms. One gets

$$\text{GVD}_{+/-} = \text{GVD}_0 \pm \frac{1}{4\kappa} \left( \frac{1}{\nu_1} - \frac{1}{\nu_2} \right) (C_1 \cdot \tilde{\omega}^2 + 1)^{-3/2} \cdot C_2, \quad (9)$$

where the functions  $C_1$  and  $C_2$  contains the terms that depend on  $D_1$ - $D_2$ :

$$C_1 = \frac{B^2}{(\nu_1 - \nu_2)^4}, \quad (10)$$

$$C_2 = \frac{4ZB + B^2 + Z^2 + 2\tilde{\omega}^2 ZB^3}{(\nu_1 - \nu_2)^4}, \quad (11)$$

with

$$B = Z + (\nu_1 - \nu_2)^2 \quad (12)$$

and

$$Z = (D_1 - D_2) \kappa \tilde{\omega} \nu_1^2 \nu_2^2. \quad (13)$$

One can expand  $C_1$  and  $C_2$  around  $\omega = \omega_0$  to the first order and get

$$C_1 \simeq 1, \quad (14)$$

$$C_2 \simeq 1 + \alpha \tilde{\omega}. \quad (15)$$

Finally, we obtain

$$\text{GVD}_{+/-} \simeq \text{GVD}_0 \pm \frac{1}{4\kappa} \left( \frac{1}{\nu_1} - \frac{1}{\nu_2} \right) (\tilde{\omega}^2 + 1)^{-3/2} (1 + \alpha \tilde{\omega}). \quad (16)$$

The introduction of a GVD difference between the two waveguides has the effect to shift the GVD peaks away from  $\omega_0$  by the introduction of an asymmetric factor which is given by

$$\alpha = \frac{6\kappa}{\delta\omega^2} (D_1 - D_2). \quad (17)$$

## OPTICAL FREQUENCY COMBS CHARACTERIZATION

Supplementary Fig. 2 shows the optical spectra measured from the reference device for a heatsink temperature of  $-15^{\circ}\text{C}$  for a current of 555, 565, 583 and 650 mA as well as the corresponding intermode beatnotes measured using a spectrum analyser with a RBW of 500 Hz. We choose this resolution bandwidth as a good compromise between resolution and acquisition time, to limit the influence of the drift during the measurement. Note that the results measured in Hugi *et al.* [3] were obtained using a real-time spectrum analyser, not a scanning instrument used here. At high currents the intermode beatnote is broad. Moreover, no multiheterodyne beating spectra could be measured from the device. This suggests that the reference device is not operating as an optical frequency comb.

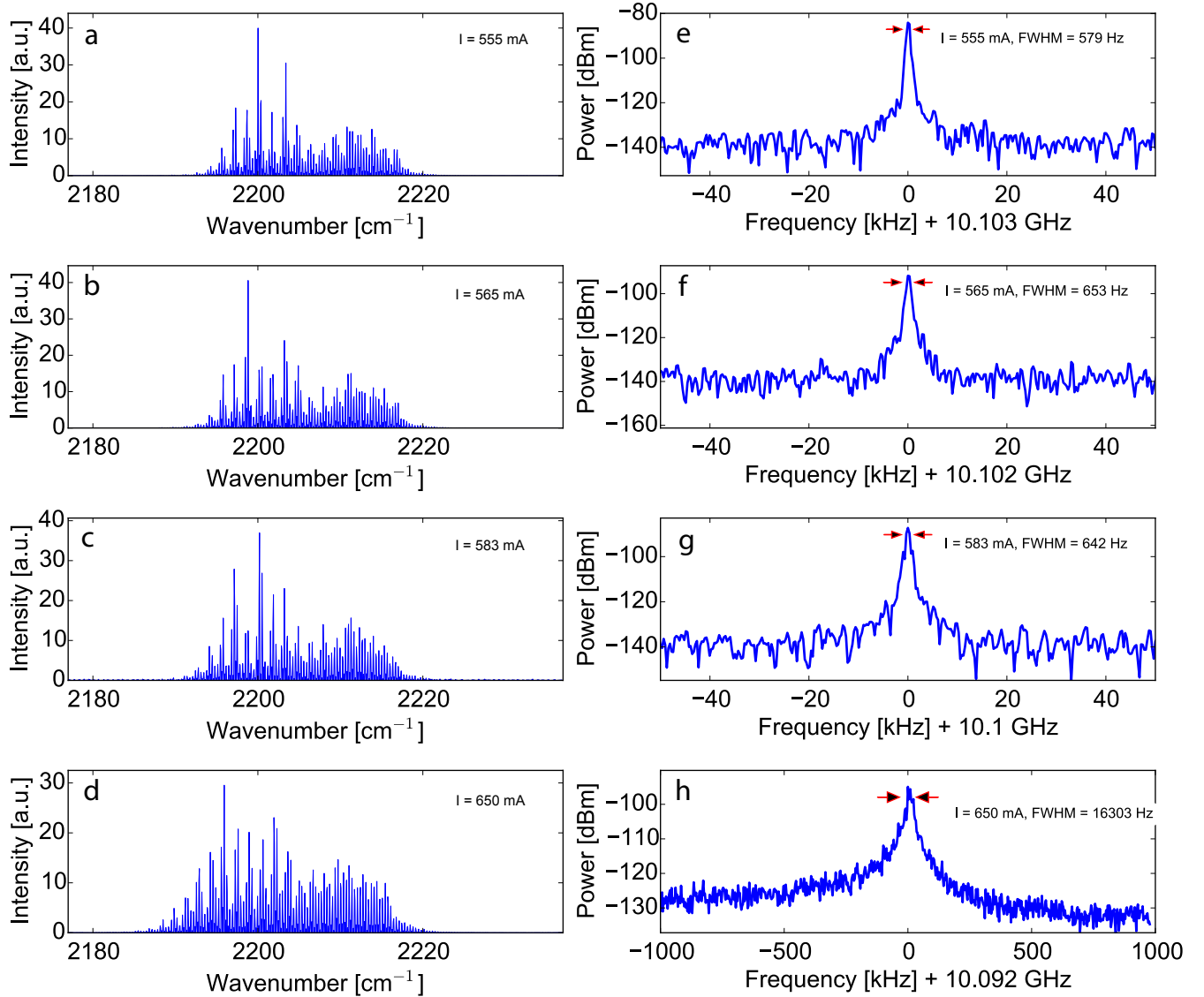


FIG. 2. **Reference laser characterization.** **a-d**, Optical spectra measured for the reference device at a heatsink temperature of  $-15^{\circ}\text{C}$  for a current of 555, 565, 583 and 650 mA. **e-h** Corresponding intermode beatnotes measured using a spectrum analyser with a RBW of 500 Hz.

Supplementary Fig. 3 shows the optical spectra measured from the coupled waveguide device for a heatsink temperature of  $-15^{\circ}\text{C}$  for a current of 720, 760, 800 and 830 mA as well as the corresponding intermode beatnotes measured using a spectrum analyser with a RBW of 500 Hz.

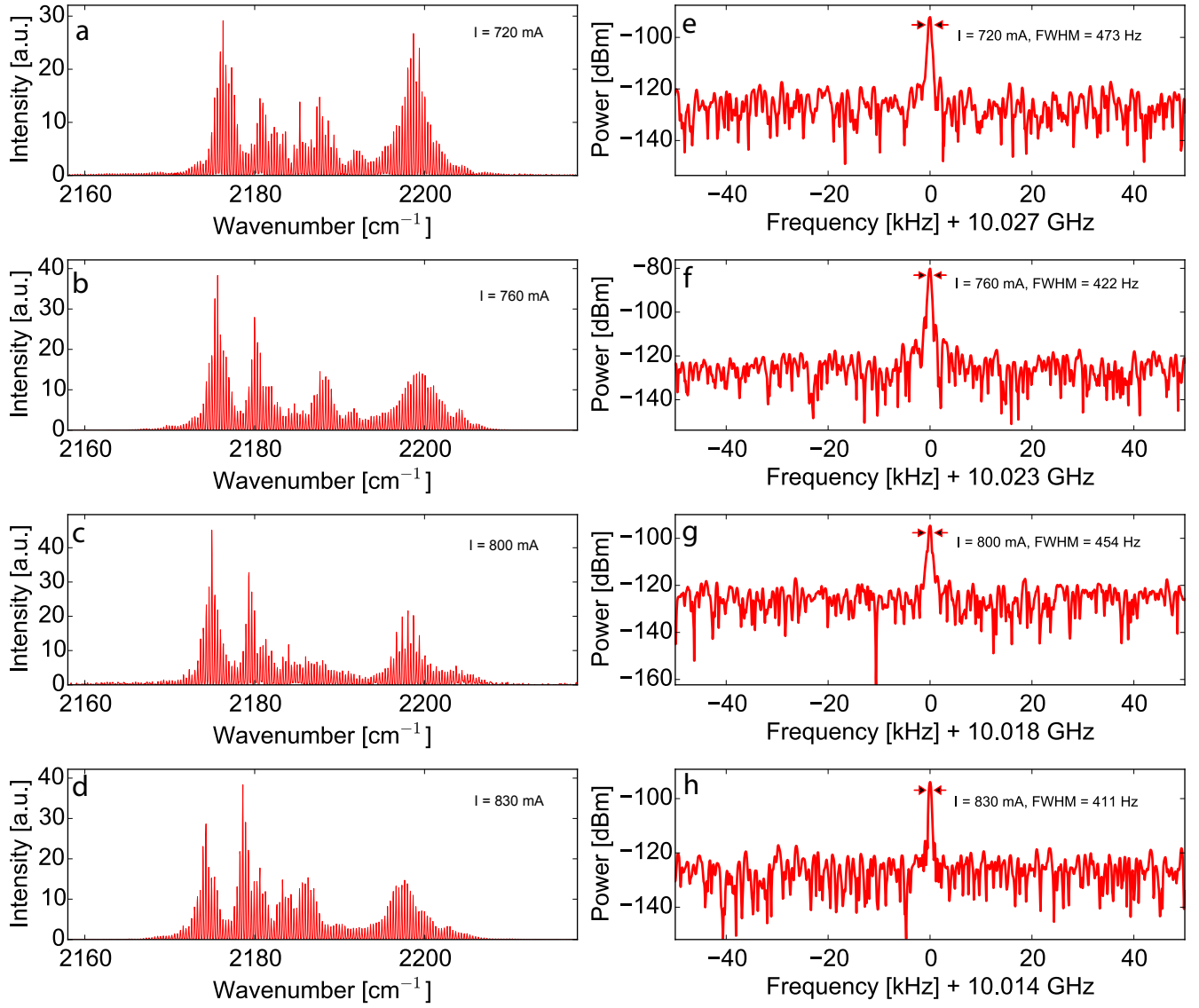


FIG. 3. **Dual waveguide laser characterization.** a-d, Optical spectra measured from the coupled waveguide device at a heatsink temperature of  $-15^{\circ}\text{C}$  for a current of 720, 760, 800 and 830 mA. e-h Corresponding intermode beatnotes measured using a spectrum analyser with a RBW of 500 Hz.

## DUAL WAVEGUIDE FOR QUANTUM-DOT LASERS

We propose a dual waveguide for GaAs/AlGaAs quantum-dot lasers. The proposed core waveguide is composed of a 643 nm thick layer  $\text{Al}_{0.15}\text{Ga}_{0.85}\text{As}$ . The core waveguide is placed in between two  $\text{Al}_{0.35}\text{Ga}_{0.65}\text{As}$  1520 nm cladding layers (Si doped  $n=10^{17} \text{ cm}^{-3}$  and C doped  $p=10^{18} \text{ cm}^{-3}$ ). A 360 nm passive GaAs waveguide is placed in the upper cladding layer at a distance  $d=700 \text{ nm}$  from the primary core waveguide. The vertical refractive index profile in the device along the growth axis is displayed in Supplementary Fig. 4a. The computed electric field profile of the anti-symmetric (blue line) and symmetric (red line) modes are also displayed, while the full two dimensional intensity profiles of these modes are reported in Supplementary Fig. 4b and c.

In Supplementary Fig. 5a, the dispersion curves of the two uncoupled modes are reported with dashed lines while the dispersion of the coupled modes are reported with full lines. Our model predicts a GVD close to zero at the laser wavelength for the anti-symmetric mode (see Supplementary Fig. 5b). The anti-symmetric mode has a higher overlap factor with the active region while the symmetric mode is localized primarily in the GaAs waveguide. In that case, mode selection results from the overlap with the active region which is larger for the anti-symmetric mode (see Supplementary Fig. 5c).

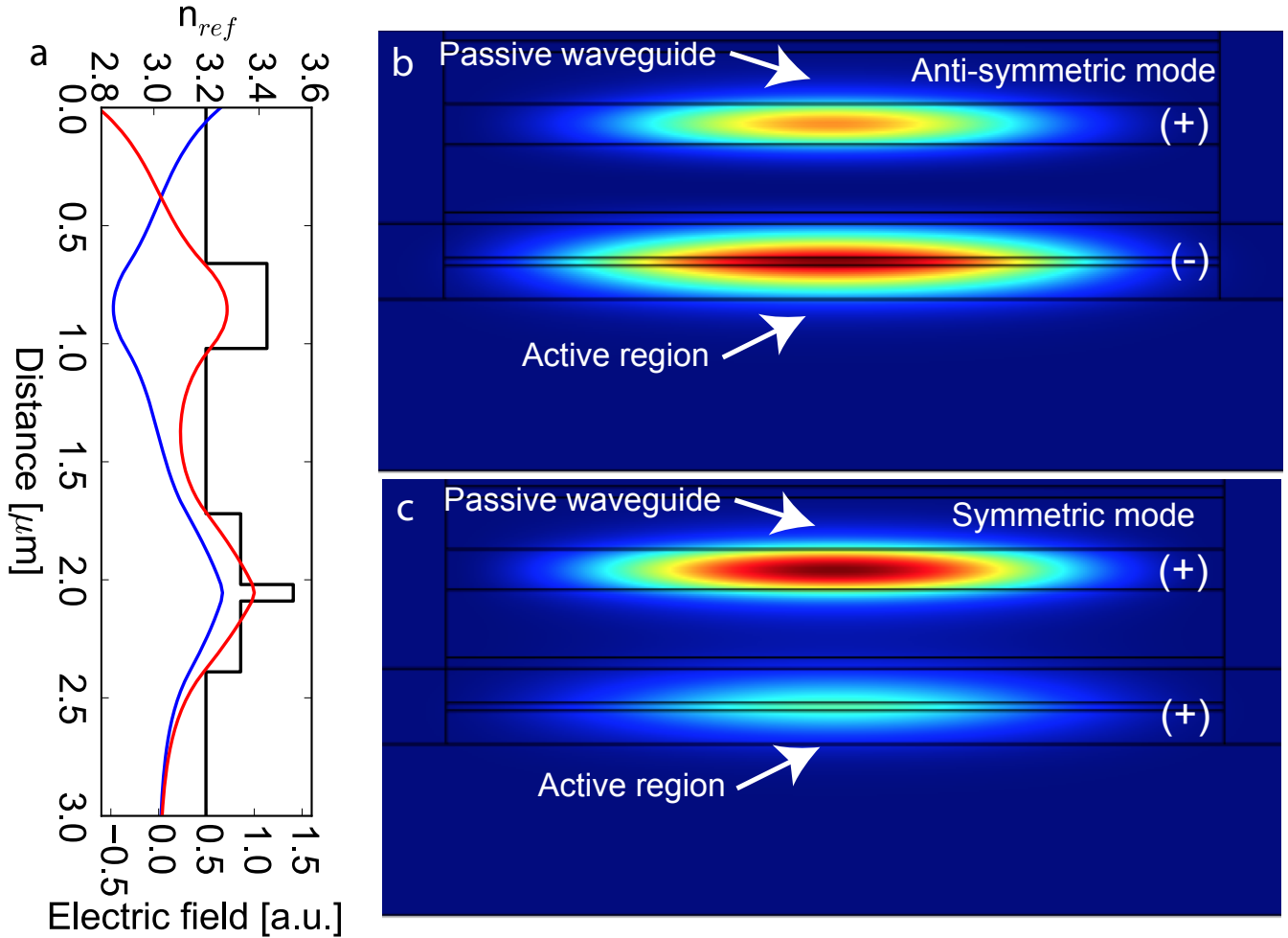


FIG. 4. **Device cross-section.** **a.** Cut in the vertical plan of the respective refractive index profile and electric field profile of the anti-symmetric (blue line) and symmetric (red line) modes. **b.** Intensity profile of the anti-symmetric mode at  $8600 \text{ cm}^{-1}$ . **c.** Intensity profile of the symmetric mode at  $8600 \text{ cm}^{-1}$ .

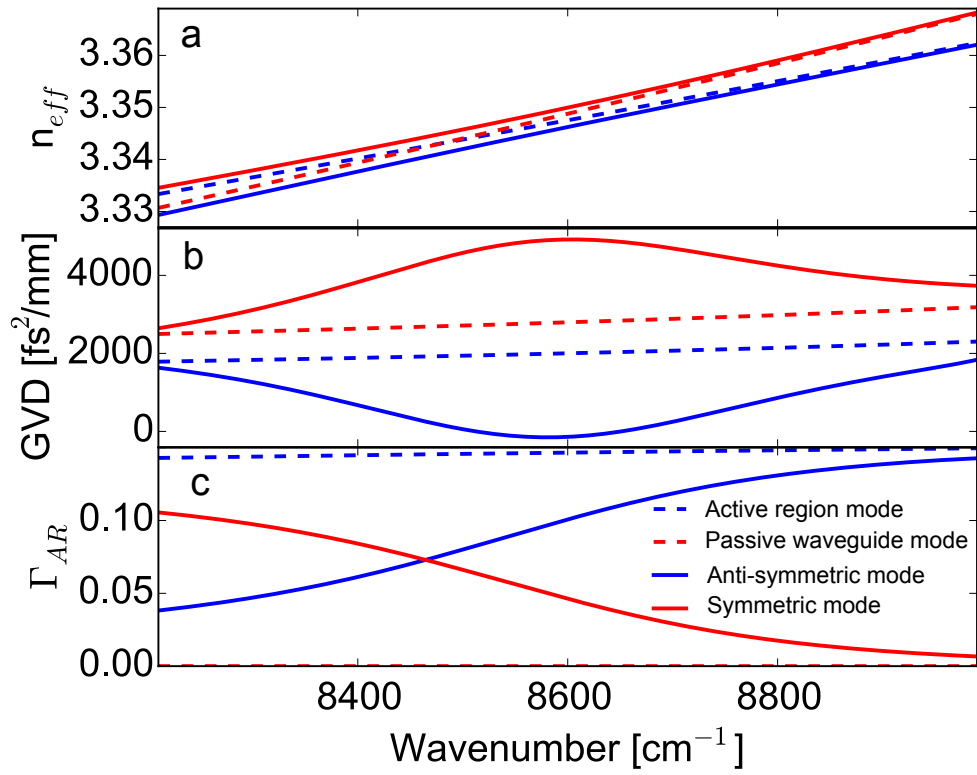


FIG. 5. **Simulation of the dispersion.** a, Spectrally resolved dispersion and b, GVD of the optical modes. c, Overlap factor with the active region.

- 
- [1] E. D. Palik and G. Ghosh, eds., *Handbook of optical constants of solids* (Academic Press, San Diego, 1998).
  - [2] U. Peschel, T. Peschel, and F. Lederer, “A compact device for highly efficient dispersion compensation in fiber transmission,” *Applied Physics Letters* **67**, 2111 (1995).
  - [3] A. Hugi, G. Villares, S. Blaser, H. C. Liu, and J. Faist, “Mid-infrared frequency comb based on a quantum cascade laser,” *Nature* **492**, 229–233 (2012).